# Accepted Manuscript

Spatially-resolved $^1$H NMR relaxation-exchange measurements in heterogeneous media

Camilla Terenzi, Andrew J. Sederman, Michael D. Mantle, Lynn F. Gladden
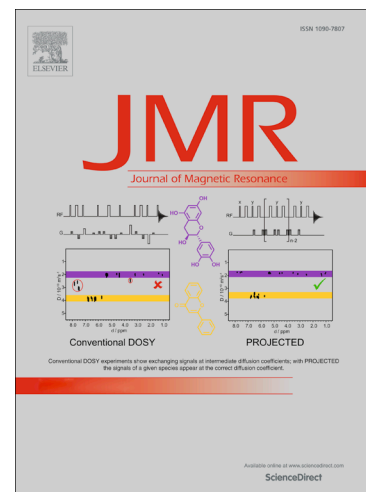
Please cite this article as: C. Terenzi, A.J. Sederman, M.D. Mantle, L.F. Gladden, Spatially-resolved $^1$H NMR relaxation-exchange measurements in heterogeneous media, *Journal of Magnetic Resonance* (2018), doi: https://doi.org/10.1016/j.jmr.2018.12.010

# Spatially-resolved $^1$H NMR relaxation-exchange measurements in heterogeneous media

Camilla Terenzi[1,§], Andrew J. Sederman[1], Michael D. Mantle[1], Lynn F. Gladden[1]

[1]Department of Chemical Engineering and Biotechnology, University of Cambridge, Philippa Fawcett Drive, Cambridge CB3 0AS, UK

[§]Present address: Biophysics Department, Wageningen University and Research, Stippeneng 4, Helix building 124, 6708WE, Wageningen, The Netherlands

1

**Abstract**

In the last decades, the $^1$H NMR $T_2 - T_2$ relaxation-exchange (REXSY) technique has become an essential tool for the molecular investigation of simple and complex fluids in heterogeneous porous solids and soft matter, where the mixing-time-evolution of cross-correlated $T_2 - T_2$ peaks enables a quantitative study of diffusive exchange kinetics in multi-component systems. Here, we present a spatially-resolved implementation of the $T_2 - T_2$ correlation technique, named $z - T_2 - T_2$, based on one-dimensional spatial mapping along $z$ using a rapid frequency-encode imaging scheme. Compared to other phase-encoding methods, the adopted MRI technique has two distinct advantages: (i) is has the same experimental duration of a standard (bulk) $T_2 - T_2$ measurement, and (ii) it provides a high spatial resolution. The proposed $z - T_2 - T_2$ method is first validated against bulk $T_2 - T_2$ measurements on homogeneous phantom consisting of cyclohexane uniformly imbibed in finely-sized α-Al$_2$O$_3$ particles at a spatial resolution of 0.47 mm; thereafter, its performance is demonstrated, on a layered bed of multi-sized α-Al$_2$O$_3$ particles, for revealing spatially-dependent molecular exchange kinetics properties of *intra-* and *inter*-particle cyclohexane as a function of particle size. It is found that localised $z - T_2 - T_2$ spectra provide well resolved cross peaks whilst such resolution is lost in standard bulk $T_2 - T_2$ data. Future prospective applications of the method lie, in particular, in the local characterisation of mass transport phenomena in multi-component porous media, such as rock cores and heterogeneous catalysts.

## 1. Introduction

Spatial variations in physico-chemical processes, such as adsorption, diffusion, capillary transport and flow, are ubiquitous in porous, condensed and soft matter. However, in most cases, an effective or averaged property is used to describe the behaviour of the system because local information cannot be obtained. It is now well-established that spatially-resolved nuclear magnetic resonance (NMR) techniques offer the opportunity to obtain a localised description from within optically-opaque media. In particular, ^{1}H NMR has been used extensively to investigate *in situ* multiphase fluid processes over a broad range of relevant spatial dimensions, from the local pore- and molecular-scales probed by 1D and 2D NMR relaxometry and diffusometry, up to the full object-sizes explored in Magnetic Resonance Imaging (MRI) [1,2]. Those complementary NMR approaches have been widely applied as separate measurements on, e.g., water/oil-bearing reservoir rocks [3], wetting/non-wetting phases in activated catalysts [4–6], hydrated cementitious or geo-polymer pastes [7], clay suspensions in natural sedimentary rocks [8], cell membranes [9] and swelling pharmaceutical tablets [10,11]. Three decades ago, the different concepts of 1D time-domain NMR and MRI were combined for the first time into multiple-echo pulse sequences based on rapid frequency-encoding imaging, to obtain real-time uniaxial $T_1$- and $T_2$-mapping for studies of colloidal filtration in rock cores [8,12–14] and for clinical applications [15–20]. Thereafter, Balcom and co-workers implemented a variety of methods for 1D $T_2$-mapping in high magnetic susceptibility media based on a pure phase-encode imaging approach, devoid of echo-time limitations and image distortions arising from signal acquisition in the presence of frequency encoding (read-out) gradients. The latter methods included CPMG-prepared SPRITE (Single Point Ramped Imaging with $T_1$ Enhancement), SE-SPI (Spin-Echo Single Point Imaging) and DANTE-Z-CPMG pulse sequences [21–24]. Among those techniques, SE-SPI provided improved temporal resolution and signal-to-noise (SNR) ratio, while shorter $T_2$ components (< 1 ms) could be accessed by CPMG-prepared SPRITE. Both techniques resulted in an improved spatial resolution (~ mm) when compared with DANTE-Z-CPMG (~ cm) and were extended by Balcom and Petrov to CPMG measurements spatially-resolved in two dimensions [25,26]. Mitchell and co-workers exploited both rapid frequency-encoded [3] and SE-SPI [27] 1D $T_2$-mapping for quantitatively monitoring oil-recovery during core floods. Diffusion MRI techniques based on filter-exchange pulse gradient spin-echo NMR

combined with slice-selective pulses were recently developed by Topgaard and co-workers [9] to map the apparent exchange rates of water in cell membranes, where distinct compartments often have poor contrast in NMR relaxation times.

The first experiment in which two time-domain dimensions were combined with a Fourier dimension was introduced by Washburn and Callaghan, with spatial resolution at the scale of local self-diffusion in 2D relaxation-exchange ($T_2 - T_2$) measurements achieved by encoding the displacement propagator [28,29]. Concurrently, Venturi and Hills introduced the first spatially-localised $T_1 - T_2$ experiment (called SPACE-$T_1 - T_2$), which combined volume-selective (*i.e.*, 3D imaging) methods with low-field 2D relaxometry [30]. The authors then exploited multi-slicing methods for single-shot acquisition of standard $T_1 - T_2$ spectra in homogeneous systems, where each slice was associated with an inversion recovery time increment [31]; the ultra-fast approach was further extended by Telkki and co-workers to diffusion-relaxation ($D - T_2$) measurements [32]. Zhang and Blümich [33] developed the first spatially-resolved $D - T_2$ correlation measurements based on the use of a 2D phase-encode imaging approach, and Balcom and co-workers [34] have implemented slice-selective 1D MRI $D - T_2$ measurements. Recently, Benjamini et al. [35] presented the first 2D MRI diffusion-exchange ($D - D$) correlation measurements in a nerve tissue phantom, obtained by combining a slice-selective 2D spin-echo MRI sequence with data under-sampling methods [36].

Among the various multi-dimensional time-domain ^{1}H NMR techniques [14] that have been developed since the first implementation of a fast numerical algorithm for 2D Inverse Laplace Transform (ILT) by Venkataramanan, Song and Hürlimann [37] and Hürlimann and Venkataramanan [38], pseudo-3D experiments for the study of diffusive exchange, like $T_2 - T_2$, represent undoubtedly the most complex and detail-rich approaches [14,39–42]. The $T_2 - T_2$ pulse sequence consists of two CPMG loops separated by a longitudinal storage period called mixing time ($\tau_{\mathrm{mix}}$), during which diffusive coupling and/or chemical exchange may take place [43–45]. Data processing via 2D ILT yields $T_2 - T_2$ correlation plots with on-diagonal intensities arising from molecules that either remain within the same local environment or undergo exchange between distinct physical domains having the same $T_2$ values during $\tau_{\mathrm{mix}}$. Cross-peaks on opposite sides of the diagonal arise from molecules that have diffused throughout sites with distinct $T_2$ relaxation environments [2]. To obtain information about mass transfer and molecular exchange kinetics, the build-up of the cross-peak intensities upon increasing $\tau_{\mathrm{mix}}$ may be analysed. Therefore, various exact and

4

numerical approaches to the analysis of multi-site $T_2 - T_2$ exchange processes inspired by chemical exchange studies [46,47] have been discussed extensively by previous workers [42,43,48–50]. A factor that complicates $T_2 - T_2$ data analysis is that, in analogy to 1D diffusion or relaxation measurements, under intermediate- or fast-exchange regimes [51] the "apparent" $T_2 - T_2$ peak positions and relative intensities can be tangibly different from their "true" values in the absence of exchange [48,52].

A number of variants of the $T_2 - T_2$ technique have been implemented in the last decade: propagator-resolved relaxation-exchange measurements [28,29,53]; compressed-sensing sampling on $T_2 - T_2$ schemes [54,55]; and faster 1D variants in the form of $T_2$-filtered $T_2 - T_2$ measurements [56]. In the following we report the first implementation and successful validation of spatially-resolved $T_2 - T_2$ relaxation-exchange measurements [2,43,44]. The experiment, here referred to as $z - T_2 - T_2$, uses a frequency-encoding scheme which enables high spatial resolution over the full sensitive region of the radio-frequency (RF) coil, while retaining the same experiment duration as in bulk $T_2 - T_2$ acquisitions. The case studies presented here show the potential of the method for localising *intra-* and *inter-*particle diffusive exchange within inhomogeneous catalyst packed beds.

## 2. Experimental

### 2.1. Materials

$\alpha$-Al$_2$O$_3$ cylindrical rings (Johnson-Matthey, PLC) with a nominal inner diameter of 2 mm, outer diameter of 5 mm, and average length of approximately 5-7 mm were used as model porous material. The surface area was ~ 5.4 m$^2$/g, and the pellets had an average porosity of 62% with a homogeneous pore-size distribution centred around $175 \pm 15$ nm, as provided by Mercury Intrusion Porosimetry (MIP). Cyclohexane (Sigma Aldrich, purity > 99.8%) was used as-received for sample preparation. The combination of macroporous $\alpha$-Al$_2$O$_3$ nearly devoid of surface hydroxyls with an apolar pore-filling liquid was chosen with the purpose of reducing the importance of surface interactions over that of diffusive coupling effects, and to detect well-resolved cross-peaks over a broad, yet experimentally accessible, $T_2$ range. Furthermore, cyclohexane is devoid of any $J$-coupling that could possibly affect the CPMG-based $z - T_2 - T_2$ measurement described in sub-section 2.2.1 [57].

To demonstrate the application of the $z - T_2 - T_2$ pulse sequence, α-Al$_2$O$_3$ cylindrical rings were crushed and sieved to different particle sizes and two distinct phantoms were prepared in 23 mm o.d. glass tubes. Phantom 1 was used for validating the method on a homogeneous assembly of fine particles, whilst phantom 2 contained a four layered vertical packing of particles with different particle size $d$, labelled in Fig. 1 as: **I**, $d < 300$ μm; **II**, 300 μm $< d < 710$ μm; **III**, 710 μm $< d < 850$ μm and **IV** with as-received cylindrical rings. Each set of particles was initially dried in oven at 105 °C overnight. For the model homogeneous phantom 1, first the dry mass was measured, then the minimum amount of cyclohexane was added to minimize excess bulk liquid content and the phantom was weighed again to estimate the amount of *intra*-particle cyclohexane uptake. Excess bulk cyclohexane was then added to completely submerge the particles, and the NMR tube was then capped and tightly wrapped with PTFE tape to prevent cyclohexane evaporation during the NMR experiments.

The same liquid loading procedure was adopted for each set of particles in phantom 2. Care was taken to ensure good sample homogeneity within the four sets of particles vertically stacked in the glass tube ensuring a nearly flat separation between adjacent layers. Regions **II** and **III** were $0.6 \pm 0.1$ cm in height, while regions **I** and **IV** was made thicker in order to align the separation between regions **II** and **III** with the centre of the FOV, as shown in Fig. 1a. Figure 1b shows a standard $^1$H 2D image of a 1 mm thick $zx$-slice taken through the centre of phantom 2 as depicted in Fig. 1a. Figure 1c shows the $^1$H NMR $z$-profile of the sample obtained by standard 1D single spin-echo frequency-encoded pulse sequence. The black dots indicate the center of the selected $z -$position within each of the four layers located at $-1.09$ cm (**I**), $-0.33$ cm (**II**), 0.33 cm (**III**), and 1.09 cm (**IV**). The labels **I**, **II**, **III** and **IV** are used for referring to the respective measured slices.
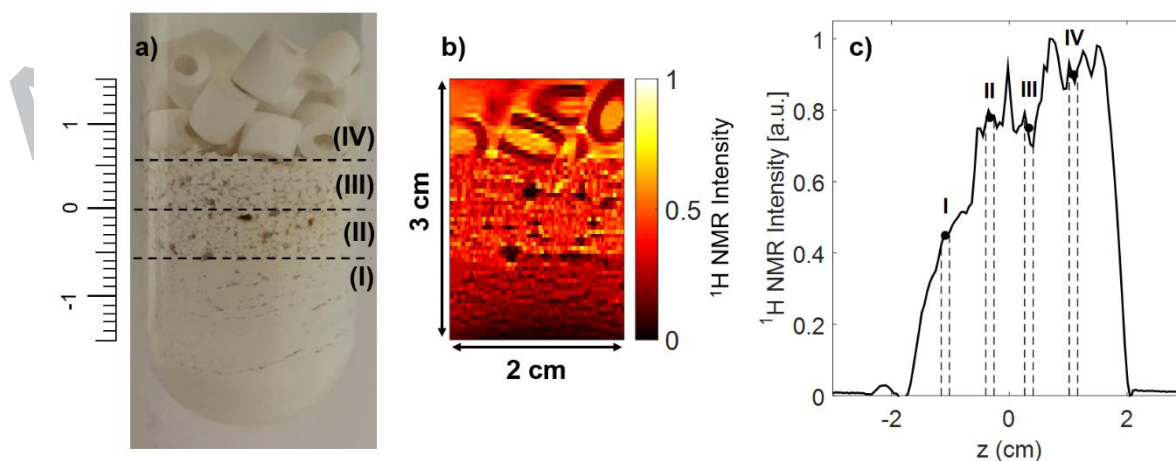


6

*Figure 1. (a) Optical image of the alumina/cyclohexane phantom used for this study. (b) 2D $^1$H NMR zx spin-echo image taken through (a). (c) 1D $^1$H NMR profile of (a) along the vertical z direction, showing the four regions described in the main text.*

We note that an average mass increase of $(61 \pm 4)$ % of the respective dry mass was measured for the fine particles of phantom 1 and for all the sets of crushed particles in phantom 2, in good agreement with the nominal porosity ($\sim 62$ %) of the $\alpha$-Al$_2$O$_3$ used here: this confirmed that, within the experimental error, uniform and nearly complete pore-filling was achieved.

## 2.2. $^1$H magnetic resonance

All $^1$H NMR measurements were performed using a Bruker AV-400 spectrometer, operating at a $^1$H resonance frequency of 400.23 MHz and equipped with a three-axis shielded gradient system that provided maximum gradient strength $G_{max} = 1.46$ T/m. A 25 mm diameter birdcage $^1$H RF coil was used for excitation and signal detection.

### 2.2.1 Implementation of the $z - T_2 - T_2$ NMR pulse sequence

Spatially-resolved $^1$H $T_2 - T_2$ exchange relaxation data [2,43,44] were acquired by using the pulse sequence illustrated in Fig. 2 which consists of two CPMG-based encoding periods for preparation and detection separated by a mixing (or storage) time of duration $\tau_{mix}$, during which molecular exchange takes place along with longitudinal relaxation. The same inter-echo spacing, namely $t_E = 3.14$ ms, was used in both CPMG loops, yielding total durations equal to $t_1 = m t_E$ and $t_2 = n t_E$, respectively. The echo index $m$ of the preparation loop was varied from 1 to 1282 in 160 steps, linearly up to the first 128 steps to fully sample up to $t_1 \sim 400$ ms, and then logarithmically up to $t_1 \sim 4$ s. For each $m$, 1024 echoes were acquired in the second CPMG loop. The duration of the 90° pulse was set to 78 μs. A 6.4 ms homospoil gradient with strength of 0.4 T/m was applied along the $x, y, z$ directions to suppress unwanted coherences during the $\tau_{mix}$ period. One-dimensional spatial-resolution was obtained along the $z$-axis, by introducing a trapezoidal dephasing gradient $G_z$ of duration $t_{dephase}$, applied between the third (restore) 90° pulse and the first 180° pulse

7

of the second CPMG loop, and a trapezoidal rephasing gradient of duration $t_{\text{rephase}}$, applied between all the $n$=1024 successive 180° pulses of the second CPMG loop.
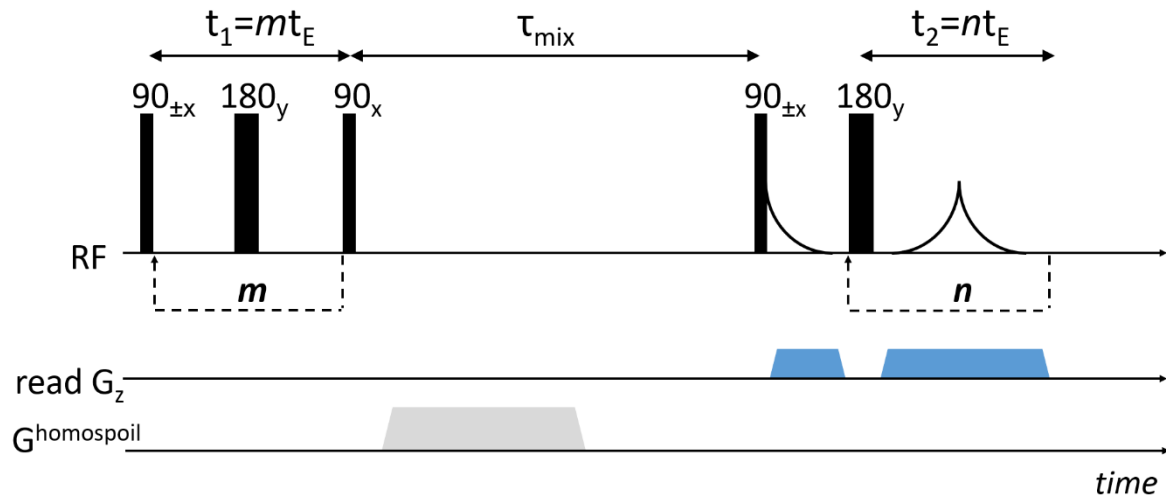


*Figure 2 - Schematic of the $z - T_2 - T_2$ pulse sequence, where frequency-encoded spin-echo $z$-profiles during the second CPMG train were recorded by applying a dephasing and a rephasing gradient in the read-direction, here $G_z$.*

The strength of the rephasing gradient was determined by the desired FOV of the performed measurements as $G_{\text{rephase}} = \frac{2\pi}{\gamma} \frac{1}{(\text{FOV} \cdot t_{\text{dw}})}$ , where $\gamma$ is the ^{1}H gyromagnetic ratio and $t_{\text{dw}}$ is the dwell-time between complex acquired points. The corresponding strength of the dephasing gradient, $G_{\text{dephase}}$, was calibrated so as to provide a dephasing gradient area equal to half that of the rephasing gradient. When necessary, a finer trim of $G_{\text{dephase}}$ was performed in order to ensure that the gradient echoes were centred within the acquisition window.

A FOV of 60 mm and sweep width of 100 kHz were chosen, producing a $G_{\text{rephase}}$ of 0.042 T/m. Hence, with $t_{\text{rephase}} = 1.71$ ms and $t_{\text{dephase}} = 0.79$ ms, as imposed by the timings for the second CPMG loop and by including a gradient ramp of 40 µs, $G_{\text{dephase}}$ was calibrated to 0.039 T/m. 256 complex points were sampled during the signal acquisition giving a spatial resolution of 0.47 mm.

Four averages were acquired according to the four-step phase-cycle shown in Fig. 2; the recycle delay was set to 13 s to enable full $T_1$ relaxation of the bulk liquid component. Data acquisition was then repeated at 18 $\tau_{\text{mix}}$ values logarithmically varied between 8 ms and 1.2 s. Each experiment took approximately 2.8 h to acquire.

### 2.2.2 2D MRI measurements

$T_2$-weighted ^{1}H images of the sample were acquired by using a multi-slice multi-echo (MSME) CPMG-based sequence (Bruker Biospin, Germany) with echo time of 3.15 ms for 8 echoes. A repetition time of 3 s was used and a $128 \times 128$ data matrix with a slice thickness 0.94 mm was acquired. For $zx$ images, the FOV was set to 60 mm and 30 mm along $z$ and $x$ directions, respectively; along $z$, the spatial resolution was set to 0.47 mm. For $xy$ (axial) images, the same acquisition parameters as above were used, but a FOV of 25 mm was chosen along both $x$ and $y$ directions. All the images were acquired in Paravision 4.0 (Bruker Biospin Ltd) and processed in MATLAB™.

### 2.3. Data Processing

Raw data were first processed in MATLAB™ in order to extract the spatially-dependent 2D matrices of correlated transverse magnetization decays. $z - T_2 - T_2$ data were Fourier-transformed in the spatial dimension and a spatially-dependent $0^{th}$-order correction of the phase, $\varphi(z)$, was applied to all the measured profiles by locally maximizing, at each $z$-position within the FOV, the respective area under the first ($m = 1$) $T_2$ decay vs. $nt_E$. The real part of the phased profiles was then retained for further data processing by 2D ILT. The noise level, provided as input for the 2D ILT algorithm, was calculated as the standard deviation of the imaginary part of the phased profiles. In order to improve the SNR, four adjacent $T_2 - T_2$ decays were added and processed by 2D ILT to obtain $T_2 - T_2$ spectra representative of a 1.42 mm thick slice, as shown in Fig. 3b.

The spatially-dependent $T_2 - T_2$ relaxation time distributions were then extracted in MATLAB™ using the mathematical method introduced by Venkataramanan et al. [37], based on singular-value decomposition [37,42,50]. Tikhonov regularization was carried out with a smoothing parameter optimized by the Generalized Cross-Validation (GCV) method described by Golub et al. [58], which yielded similar smoothing coefficients for both bulk and spatially-resolved datasets.

For each $T_2 - T_2$ spectrum, on-diagonal and cross-peak integral intensities were calculated by volumetric integration of the signal density within manually-selected rectangular regions-of-interest (ROIs) centred around each detected peak. To analyse

diffusive-exchange within the sample, the total intensity of cross peaks in each $T_2 - T_2$ spectrum of regions **I** and **II** was normalized to its total integral area. The exchange kinetics were fitted by using the Levenberg-Marquardt algorithm with single-exponential functions [14,43] yielding an effective exchange time $\tau_{ex,eff}$, where the $T_1^{-1}$ correction to $\tau_{ex,eff}^{-1}$ proposed by Washburn and Callaghan [43] proved negligible within the fitting error.

## 3. Results and discussion

### 3.1. Validation of the $z - T_2 - T_2$ measurements

Figure 3 shows the results of the validation test of the $z - T_2 - T_2$ technique for phantom 1 consisting of the finely-sized α-Al$_2$O$_3$ particles with $d < 300$ μm, equivalent to those within region **I** of the phantom 2. Figure 3a shows the spatially unresolved $T_2 - T_2$ plot, whilst Figs. 3b and 3c both show the $z - T_2 - T_2$ results obtained, respectively, from a 1.42 mm thick slice (region **I**) and from the whole sensitive region of the coil (~ 3.1 cm). For Fig. 3c, the global $T_2 - T_2$ plot was reconstructed by processing the sum of all the individual $z - T_2 - T_2$ decays within the 3.1 cm region.
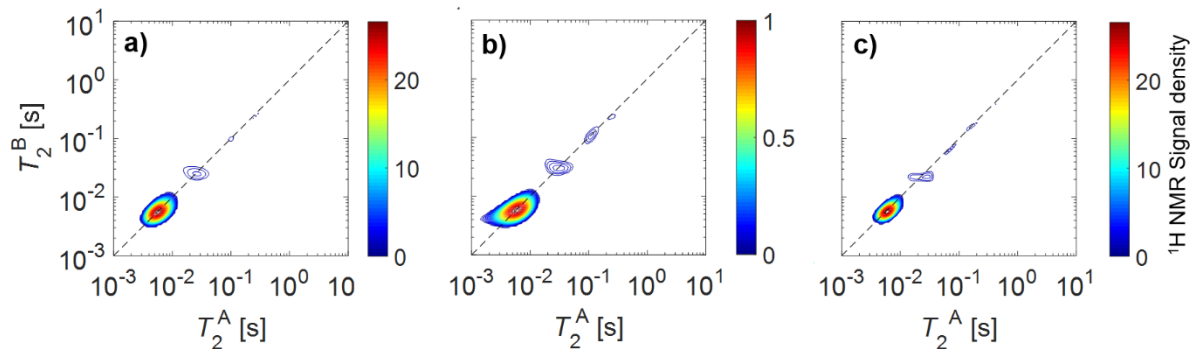


*Figure 3. $T_2 - T_2$ correlation plots for phantom 1 at $\tau_{mix}$ = 8 ms, obtained from: (a)spatially unresolved $T_2 - T_2$ data; (b) $z - T_2 - T_2$ data corresponding to the position of region **I** in Fig. 1c; (c) the sum of all $z - T_2 - T_2$ data within the sensitive region of the coil (~3.1 cm).*

All three correlation maps in Fig. 3, where $T_2^B$ represents the direct dimension and $T_2^A$ the indirect one, respectively sampled during the $n$ and $m$ loops in Fig. 1, exhibit nearly identical ^{1}H signal-density features and resolution of peaks.. The lack of artefacts due to the signal acquisition in the presence of read-out gradients fully validates the $z - T_2 - T_2$ methodology against the

10

bulk $T_2 - T_2$ experiment and also confirms the validity of the data processing of the spatially-resolved data with 2D ILT.

No cross-peaks are observed in Fig. 3 as a result of negligible diffusive exchange at such a short $\tau_{\text{mix}}$ value of 8 ms. The most intense population lies along the diagonal line with $T_2 = 5.8$ ms, and three more on-diagonal peaks of progressively smaller intensity are observed at approximately 20 ms, 60 ms and 200 ms. The assignment of such populations is discussed in detail for the multi-layered phantom 2 in the forthcoming section.

### 3.2. Spatially resolved $T_2 - T_2$ exchange

Figure 4a shows a series of 1 mm thick two-dimensional $xy$-slice images taken through phantom 2 at positions **I**, **II**, **III** and **IV**. The individual crushed particles in layers **I**, **II** and **III** are not discernible in the images as they are smaller than, or comparable to, the image resolution of 195 $\times$195 $\times$ 940 μm; a number of air bubbles are also observed as black areas in the images. The differences in $^1$H signal intensity visible in the $^1$H 2D $xy$-images is due to a number of factors: (i) significant $T_2$ relaxation effects for intra particle liquid; (ii) variations in local porosity and (iii) background magnetic field susceptibility gradients; (iv) the addition of a repeated readout gradient will cause additional signal attenuation which may have to be taken into account in high resolution or long $T_2$ systems. In the current implementation, the effect of the readout gradient is small and results in a reduction of the longest measured $T_2$ (~500 ms) of less than 3% of its true value, and has a smaller effect on shorter $T_2$ values.

The first four vertical panels of Fig. 4 show the $z - T_2 - T_2$ results, respectively from regions **I** to **IV**, whilst the rightmost panel shows the corresponding spatially-unresolved (bulk) $T_2 - T_2$ data; along the horizontal rows, Figs. 4b-4e show the results obtained at $\tau_{\text{mix}} = 8$, 60, 118 and 231 ms. We note that figs. 4b and 3a are from ostensibly similar samples and show good agreement, but that small differences may be expected to occur due to small differences in packing and particle size distributions. The $z - T_2 - T_2$ plots at $\tau_{\text{mix}} = 8$ ms (see Fig. 4b) show four on-diagonal populations labelled **A**, **B C** and **D**, whose $T_2$ values and relative populations are summarized in Table 1.

An important point to consider to facilitate the physical interpretation of peaks **A**, **B** and **C** in the $z - T_2 - T_2$ exchange plots in Figs. 4b-4e is the length scale of diffusional averaging. The self-diffusion coefficient of cyclohexane, *D*, for phantom 2 was measured by PFG-NMR (data not shown) to be 0.6-0.9 $\times 10^{-9}$ m$^2$/s. By taking into account the relaxation time values of population **A**, $T_2(A) \sim 5.8$ ms, and of the bulk-like population **D**, $T_2(D) \sim 0.49$

11

s, the molecular displacement ranges between $l_D(A) = \sqrt{DT_2(A)} \sim 1.9\text{-}2.3$ μm to $l_D(D) = \sqrt{DT_2(D)} \sim 17\text{-}20$ μm [59]. This range of length scale defines the upper limit of the diffusion length above which structural heterogeneities experienced by the confined liquid are not averaged out during the NMR observation time-scale and therefore gives rise to multi-exponential relaxation. Hence, the multi-site $T_2 - T_2$ spectra necessarily reflect structural and/or dynamic heterogeneities at spatial scales larger than a few microns, which is significantly larger than the *intra*-particle pore-size of the particles. We now discuss the assignment of peaks **A**, **B**, **C** and **D**.
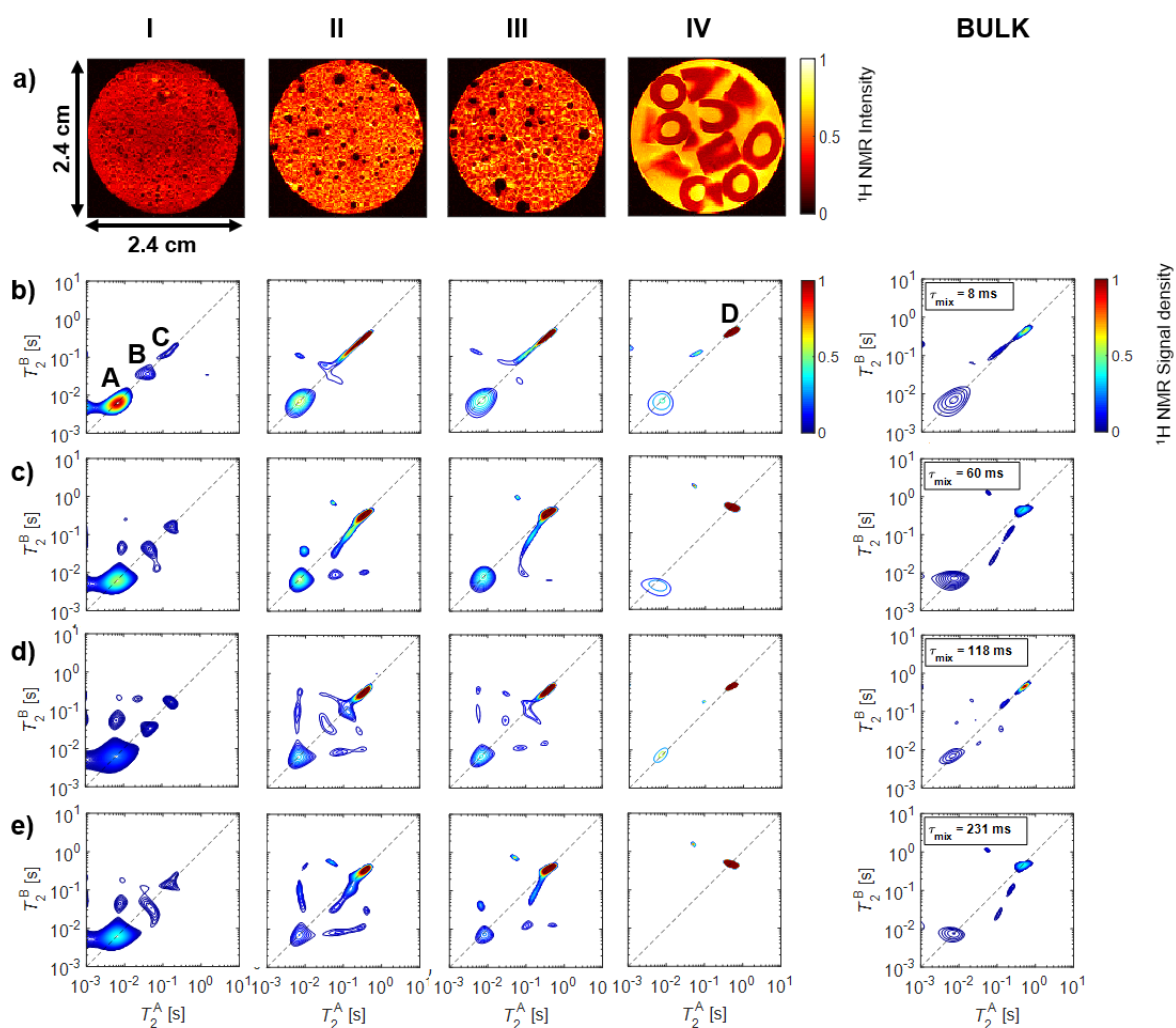


*Figure 4. For phantom 2, NMR data from left to the second rightmost column refer to regions with increasing particles sizes. In (a) 2D axial $^1H$ NMR images are shown for each region of the sample. In (b), (c), (d) and (e), $z - T_2 - T_2$ relaxation-exchange maps acquired with $\tau_{mix} = 8, 60, 118$ and $231$ ms respectively, are shown. All $^1H$ signal density scales are normalized to the maximum intensity in the second rightmost plot of (b). The rightmost panel*

*shows the 2D ILT results obtained for the sum of all time-domain data within the sensitive region of the coil (~ 3.1 cm): the signal density scale is normalised to that at $\tau_{mix} = 118$ ms.*

**Table 1** $T_2$ values (ms) for phantom 2 for on-diagonal peaks **A**, **B**, **C** and **D**, and corresponding signal populations (%), normalized to the total signal intensity for each 2D relaxation-exchange plot for $\tau_{mix} = 8$ ms. The percentage measurement error on $T_2$ is around 5%. [*] The total percentage intensity is less than 100 due to the presence of small cross-peaks even at short $\tau_{mix}$.

| Packing region | $T_2$ /ms [Relative population %] | | | |
|---|---|---|---|---|
| | **A** | **B** | **C** | **D** |
| **I** | 6.1 [92] | 40 [5] | 132 [3] | - |
| **II**[*] | 7.1 [46] | - | 126 [17] | 336 [34] |
| **III** | 7.1 [49] | - | 126 [14] | 404 [37] |
| **IV** | 7.1 [38] | - | - | 487 [62] |

Peak **A** for region **I** in Fig. 4b ($\tau_{mix} = 8$ ms) is due to overlapping contributions from *intra*-particle cyclohexane and *inter*-particle cyclohexane diffusing in the smallest *inter*-particle voids: both such environments are presumably largely influenced by background magnetic susceptibility field gradients on length scales smaller than $l_D$. Peaks **B** and **C** in region **I** ($\tau_{mix} = 8$ ms) for Fig. 4b represent a small fraction of the total cyclohexane molecules, namely ~ 8%, that reside solely in *inter*-particle void spaces of the catalyst packing whose mean void sizes are considerably larger than the diffusive length scale of ~ 1.4-1.7 μm. As a consequence, these liquid populations are both less motionally-hindered and less affected by background magnetic susceptibility gradients as compared to peak **A**, thus resulting in larger $T_2$ values. The fact that two distinct peaks (**B** and **C**) are observed would normally indicate the presence of a distinct bi-modal *inter*-particle size space. However, this is physically unlikely given the adopted sample preparation method. Furthermore, because peaks **B** and **C** have poor SNR in region **I**, "pearling" artefacts typical of 2D ILT on the observed peak splitting cannot be excluded. This consideration is supported by the fact that peaks **B** and **C** tend to merge into a single broad feature in the $z - T_2 - T_2$ plots for regions **II** and **III** at $\tau_{mix} = 8$ ms. The increase in the ^{1}H signal integral intensity from region **I** to region **III** (see Table 1) reflects the increase in the average size of the *inter*-particle void space, and subsequent decrease in external particle surface area at lower packing densities. In

13

region **IV**, where small *inter*-particle voids are essentially absent, peak **A** results predominantly from *intra*-particle cyclohexane and Peak **D** arises from free cyclohexane that is uninfluenced by the alumina particles. We do note a small, but significant, population located near the diagonal at $T_2 \sim 100$ ms, which is attributed to a minor amount of cyclohexane in direct contact with the surfaces of the large alumina rings in region **IV**. The decrease in the relative population of peak **A**, from ~ 92% in region **I** to ~ 38% in region **IV**, is predominantly attributed to the reduced density of *intra*-particle pores in region **IV** relative to region **I** and inter particle cyclohexane located within $l_D$ of the particles.

Upon increasing $\tau_{mix}$, as shown in Figs. 4c-4e, multi-site cross-peaks are observed for all crushed particles (regions **I**-**III**) but are essentially absent in region **IV**. The appearance of cross-peaks is indicative of molecular exchange between two physically different environments with different $T_2$ relaxation properties. In region **I** cross-peaks are visible only above the diagonal, yielding an asymmetric $T_2 - T_2$ signal density profile. The origin of asymmetry of the intensity of $T_2 - T_2$ cross peaks in three-site exchange systems with non-identical exchange times, and hence equilibrium populations, has been discussed by van Landeghem *et al*. [48] in terms of the mass balance rule being valid on the overall system, but not within each sub-set of two-site exchanging domains. This is the case of our system, where the spin population of peak **A** is much larger than that of peak **B**, resulting in a pronounced molecular exchange time asymmetry $\tau_{AB} \gg \tau_{BA}$ [14,48]. In addition, population **A** is more $T_1$-weighted (data not shown), resulting in *BA* cross-peak intensities, below the diagonal line, decaying more quickly than *AB* ones, above the diagonal line, as $\tau_{mix}$ increases. Indeed, we note that in region **II**, where (i) on-diagonal peaks are more evenly populated and (ii) population **D**, with least $T_1$-weighting effects, becomes larger, the cross-peaks are more symmetric. Other sources of asymmetry in our system might be due to the effects of Laplace inversion procedure on peaks with low SNR.

In region **III** at $\tau_{mix}$= 8 ms, peak **A** has a much-reduced population compared to region **I**, and additionally undergoes larger $T_1$-weighting as $\tau_{mix}$ increases from 8 ms to 231 ms compared to the other on-diagonal intensities. The cross-peak intensities are reduced relative to region **I** because the larger voids in region **III** result in a smaller solid surface area available for molecular exchange.

The rightmost panel in Fig. 4 shows the $z - T_2 - T_2$ plots for the whole sample obtained by summing all the time-domain data over the homogeneous region of the coil (~ 3.1 cm). Interestingly, as opposed to localised $z - T_2 - T_2$ plots in Fig. 4, in such bulk spectra cross-peaks are difficult to identify due to their low SNRs, and no substantial evolution with $\tau_{mix}$ is observed. This is due to the fact that, upon summing the decays from

14

all layers of particles, the overwhelming contribution to the $T_2 - T_2$ plots from mobile cyclohexane in regions **III** and **IV** completely masks the low-intensity cross-peaks characteristics of regions **I** and **II**. The comparison between bulk and localised $z - T_2 - T_2$ spectra shows that, in such macroscopically heterogeneous system, the bulk $T_2 - T_2$ technique cannot resolve low-intensity exchange cross-peaks, whilst such information is fully retained in localised $z - T_2 - T_2$ spectra, alongside spatial selectivity. In the following, the discussion and analysis of molecular exchange in regions **I** and **II** will be further analysed.

Figures 5a and 5b illustrate, for particles in region **I**, the evolution vs. $\tau_{\mathrm{mix}}$ of the normalized diagonal integral intensity of peak **A**, indicated as $I^{\mathrm{AA}}/I^{\mathrm{tot}}$, and of the normalized **AB** cross-peak integral intensity, indicated as $I^{\mathrm{AB}}/I^{\mathrm{tot}}$, where $I^{\mathrm{tot}}$ is the total intensity of the $z - T_2 - T_2$ spectrum. Figures 5c and 5d report similar information for region **II**, where $I^{\mathrm{AB}}$ is replaced by the total intensity of all cross-peaks, $I^{\mathrm{XP}}$. A two-parameter single-exponential fitting based on the Levenberg-Marquardt least-square minimisation algorithm (black solid curves) was performed, in Figs. 5a and 5c, via the function $\frac{I^{AA}}{I^{tot}} = \frac{I^{AA}(0)}{I^{tot}(0)} \cdot exp\left(-\frac{\tau_{mix}}{\tau_{ex,eff}^{AA}}\right)$ or, in Figs.5b and 5d, via the single-exponential recovery $\frac{I^{AB(XP)}}{I^{tot}} = \frac{I^{AB(XP)}(\infty)}{I^{tot}(\infty)} \cdot \left[1 - exp\left(-\frac{\tau_{mix}}{\tau_{ex,eff}^{AB(XP)}}\right)\right]$ [14,43].
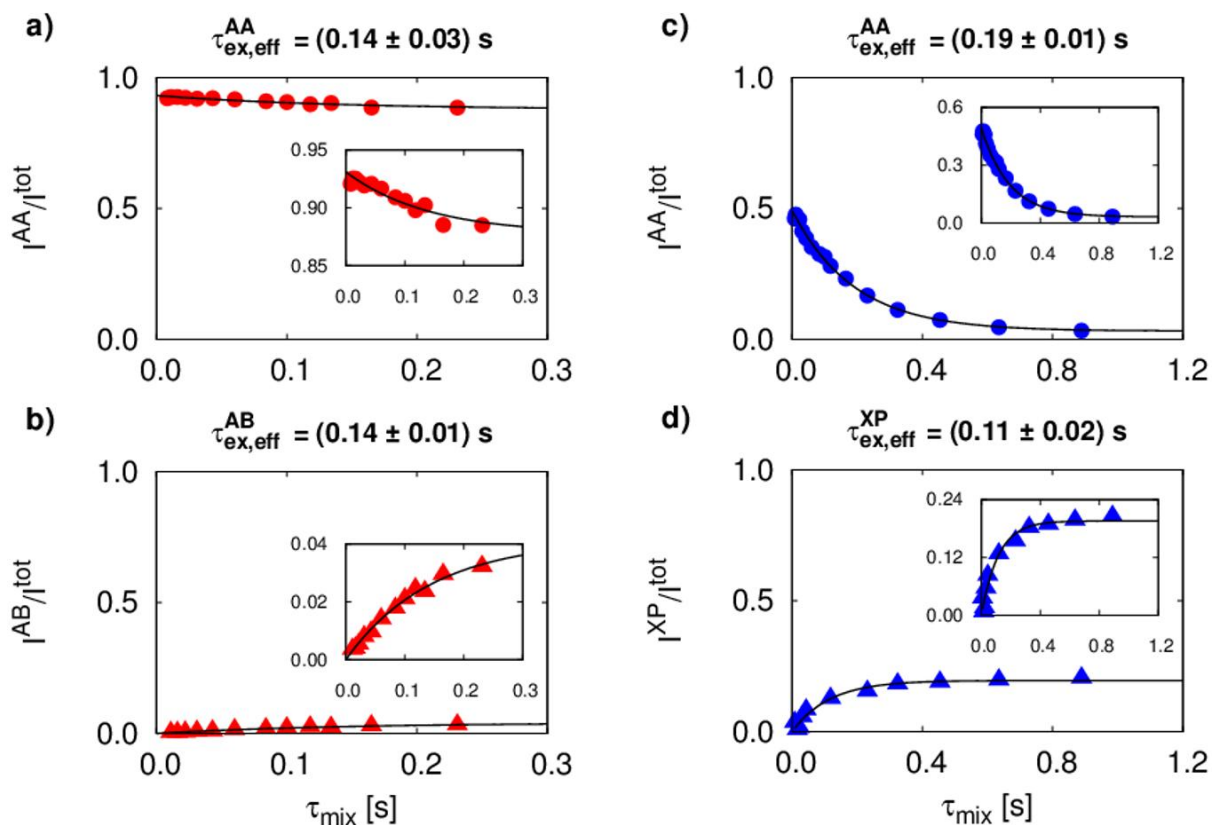
15

*Figure 5 - The evolution of $^1H$ signal intensity vs. $\tau_{mix}$ for: (a) normalized integral intensity of peak A, and (c) the normalized cross-peak intensity $I^{AB}$. (b) and (d) as for (a) and (c), but for data from region II. In (d), the cross-peak intensity $I^{XP}$ refers to the sum of all the off-diagonal peaks.*

For region **I**, data were fitted up to $\tau_{mix}$ of 0.3 s, and yielded identical "effective", *i.e.* without $T_1$-correction [43], exchange times, namely $\tau_{ex,eff}^{AA} \sim \tau_{ex,eff}^{AB} \sim 0.14$ s. This confirms the substantial two-site nature of exchange in region **I**, as was expected considering the very low intensity of peak **C** and of its cross-peaks. Seven-parameter fitting of the non-normalized cross-peak intensity ($I^{AB}$) by using the matrix representation proposed by Dortch et al. [49], inclusive of both $T_1$ and $T_2$ relaxation, provided $\tau_{ex,eff}^{AB,corr} = \left(\frac{1}{\tau_{AB}} + \frac{1}{\tau_{BA}}\right)^{-1} = (0.16 \pm 0.03)$ s, coincident within the error with the above estimate obtained by a more robust two-parameter fitting.

Figures 5c and 5d show that, in region **II** and up to $\tau_{mix}$ values of about 1.2 s, single-exponential decays with approximately similar exchange rates as in region **I** were obtained for both $I^{AA}/I^{tot}$ and $I^{XP}/I^{tot}$. This shows that all individual pairs of exchanging liquid

16

domains in region **II** undergo molecular exchange with similar average rates, resulting in an overall single-exponential behaviour.

Notably, fig. 5b shows that the amount of liquid exchanging between **A** and **B** sites in region **I** is very small, only about 4% of the total intensity, when compared to the larger liquid fraction of ~ 20%, in fig. 5d for peak **A**, in region **II**. If diffusive exchange with population **A** in crushed particles were dominated by the *intra*-particle liquid component in **A**, one would observe a decrease in the net amount of exchanged liquid from region **I** to region **II**, due to correspondingly lower density of particles. Instead, the increase by a factor of about 5 in the $I^{\text{XP}}/I^{\text{tot}}$ and $I^{\text{AA}}/I^{\text{tot}}$ values at equilibrium conditions, i.e. at longest $\tau_{\text{mix}}$ values in Figs. 5b and 5d, is consistent with the scaling factor of about 3-5 in the average particle sizes, and hence mean *inter*-particle distances, when going from region **I** to region **II**. This latter result, in line with the fact that *intra*-particle exchange is likely to be completely averaged out at our diffusion length scales of $l_{\text{D}} = \sim 1.4\text{-}1.7$ µm (see section 3.2), ultimately confirms the pure *inter*-particle character of the multi-site diffusive exchange under study.

## 4. Conclusions

In this work we have introduced a novel and efficient ¹H NMR methodology, named $z - T_2 - T_2$, for performing a spatially-resolved acquisition of $T_2 - T_2$ relaxation-exchange spectra based on the use of 1D frequency-encoding magnetic field gradients. A model system consisting of macroporous α-Al$_2$O$_3$ imbibed with cyclohexane was used and the spatially resolved data showed no artefacts due to the presence of frequency-encoding gradients, when compared with bulk $T_2 - T_2$ methods.

The $z - T_2 - T_2$ technique was used to characterise the molecular exchange times of a liquid imbibed in porous media, and was demonstrated on a phantom comprising a multi-layered packing of α-Al$_2$O$_3$ with particle sizes varying spatially from < 300 µm up to ~1 cm along the direction of the MRI resolution, containing both *intra-* and *inter*-particle cyclohexane. In such heterogeneous packing, the use of localised $z - T_2 - T_2$ measurements at varying mixing-time proved essential, not only for obtaining a spatially-resolved characterization of *inter*-particle liquid exchange, but also for revealing cross-peaks that could not observed at all in overall bulk $T_2 - T_2$ spectra. This result fully demonstrates the significant advantages of the new proposed method over conventional $T_2 - T_2$ measurements.

The proposed $z - T_2 - T_2$ method will likely be of use in characterising mass transport phenomena in a variety of different research environments including petrochemical, pharmaceutical and catalysis research. Here, a quantitative knowledge of multi-scale spatially dependent fluid mass transport processes that occur between the *intra-* and *inter-*particle pore space in laboratory scale experiments, will provide useful information when designing pilot scale operations.

## Acknowledgements

## References

[1]     R. Kimmich, NMR: Tomography, Diffusometry, Relaxometry, Springer-Verlag, Berlin, 1997.

[2]     P. T. Callaghan, Translational Dynamics and Magnetic Resonance: Principles of Pulsed Gradient Spin Echo NMR, Oxford University Press, New York, 2011.

[3]     J. Mitchell, J. Staniland, R. Chassagne, E.J. Fordham, Quantitative in situ enhanced oil recovery monitoring using nuclear magnetic resonance, Transp. Porous Media. 94 (2012) 683–706.

[4]     M.D. Mantle, A.J. Sederman, Dynamic MRI in chemical process and reaction engineering, Prog. Nucl. Magn. Reson. Spectrosc. 43 (2003) 3–60.

[5]     B. Newling, Gas flow measurements by NMR, Prog. Nucl. Magn. Reson. Spectrosc. 52 (2008) 31–48.

[6]     F. Dalitz, M. Cudaj, M. Maiwald, G. Guthausen, Process and reaction monitoring by low-field NMR spectroscopy, Prog. Nucl. Magn. Reson. Spectrosc. 60 (2012) 52–70.

[7]     J.-P. Korb, NMR and nuclear spin relaxation of cement and concrete materials, Curr. Opin. Colloid Interface Sci. 14 (2009) 192–202.

[8]     E.J. Fordham, M.A. Horsfield, L.D. Hall, G.C. Maitland, Depth filtration of clay in rock cores observed by one-dimensional ^{1}H NMR imaging, 1993.

[9]     S. Lasič, M. Nilsson, J. Lätt, F. Ståhlberg, D. Topgaard, Apparent exchange rate mapping with diffusion MRI, Magn. Reson. Med. 66 (2011) 356–365.

[10]    M.D. Mantle, Quantitative magnetic resonance micro-imaging methods for pharmaceutical research, Int. J. Pharm. 417 (2011) 173–195.

[11]    M.D. Mantle, NMR and MRI studies of drug delivery systems, Curr. Opin. Colloid Interface Sci. 18 (2013) 214–227.

[12]    E.J. Fordham, A. Sezginer, L.D. Hall, Imaging multiexponential relaxation in the (y, $Log_e T_1$) plane, with application to clay filtration in rock cores, J. Magn. Reson. Ser. A. 113 (1995) 139–150.

[13]  M.A. Horsfield, E.J. Fordham, C. Hall, L.D. Hall, ^{1}H NMR imaging studies of filtration in colloidal suspensions, J. Magn. Reson. 81 (1989) 593–596.

[14]  J. Mitchell, L.F. Gladden, T.C. Chandrasekera, E.J. Fordham, Low-field permanent magnets for industrial process and quality control, Prog. Nucl. Magn. Reson. Spectrosc. 76 (2014) 1–60.

[15]  T.J. Mosher, B.J. Dardzinski, Cartilage MRI $T_2$ relaxation time mapping: overview and applications, Semin. Muskoskeletal Radiol. 8 (2004) 355–368.

[16]  C.S. Poon, R.M. Henkelman, Practical $T_2$ quantitation for clinical-applications, J. Magn. Reson. Imaging. 2 (1992) 541–553.

[17]  G. Saab, R. Terry Thompson, G.D. Marsh, P.A. Picot, G.R. Moran, Two-dimensional time correlation relaxometry of skeletal muscle in vivo at 3 tesla, Magn. Reson. Med. 46 (2001) 1093–1098.

[18]  G. Saab, R.T. Thompson, G.D. Marsh, Multicomponent $T_2$ relaxation of in vivo skeletal muscle, Magn. Reson. Med. 42 (1999) 150–157.

[19]  S.J. Graham, M.J. Bronskill, MR measurement of relative water content and multicomponent $T_2$ relaxation in human breast, Magn. Reson. Med. 35 (1996) 706–715.

[20]  M.D. Does, J.C. Gore, Compartmental study of $T_1$ and $T_2$ in rat brain and trigeminal nerve in vivo, Magn. Reson. Med. 47 (2002) 274–283.

[21]  O. V. Petrov, B.J. Balcom, Local $T_2$ distribution measurements with DANTE-Z slice selection, J. Magn. Reson. 215 (2012) 109–114.

[22]  O. V. Petrov, G. Ersland, B.J. Balcom, $T_2$ distribution mapping profiles with phase-encode MRI, J. Magn. Reson. 209 (2011) 39–46.

[23]  S. Vashaee, F. Marica, B. Newling, B.J. Balcom, A comparison of magnetic resonance methods for spatially resolved $T_2$ distribution measurements in porous media, Meas. Sci. Technol. 26 (2015) 055601-16.

[24]  L. Li, H. Han, B.J. Balcom, Spin echo SPI methods for quantitative analysis of fluids in porous media, J. Magn. Reson. 198 (2009) 252–260.

[25]  O. V. Petrov, B.J. Balcom, Two-dimensional $T_2$ distribution mapping in porous solids with phase encode MRI, J. Magn. Reson. 212 (2011) 102–108.

[26]  D. Xiao, B.J. Balcom, Two-dimensional $T_2$ distribution mapping in rock core plugs with optimal k-space sampling, J. Magn. Reson. 220 (2012) 70–78.

[27]  J. Mitchell, J. Staniland, R. Chassagne, K. Mogensen, S. Frank, E.J. Fordham, Mapping oil saturation distribution in a limestone plug with low-field magnetic resonance, J. Pet. Sci. Eng. 108 (2013) 14–21.

[28]  K.E. Washburn, C.H. Arns, P.T. Callaghan, Pore characterization through propagator-resolved transverse relaxation exchange, Phys. Rev. E - Stat. Nonlinear, Soft Matter Phys. 77 (2008) 051203-13.

[29]  K.E. Washburn, P.T. Callaghan, Propagator resolved transverse relaxation exchange spectroscopy, J. Magn. Reson. 186 (2007) 337–340.

[30]  L. Venturi, B. Hills, Spatially resolved multidimensional cross-correlation relaxometry, Magn. Reson. Imaging. 28 (2010) 171–177.

[31]  L. Venturi, J. Warner, B. Hills, Multisliced ultrafast 2D relaxometry, Magn. Reson. Imaging. 28 (2010) 964–970.

[32]    S. Ahola, V. V. Zhivonitko, O. Mankinen, G. Zhang, A.M. Kantola, H.-Y. Chen, C. Hilty, I. V. Koptyug, V.-V. Telkki, Ultrafast multidimensional Laplace NMR for a rapid and sensitive chemical analysis, Nat. Commun. 6 (2015) 8363.

[33]    Y. Zhang, B. Blümich, Spatially resolved D-$T_2$ correlation NMR of porous media, J. Magn. Reson. 242 (2014) 41–48.

[34]    S. Vashaee, B. Newling, B. MacMillan, F. Marica, M. Li, B.J. Balcom, Local diffusion and diffusion-$T_2$ distribution measurements in porous media, J. Magn. Reson. 278 (2017) 104–112.

[35]    D. Benjamini, M.E. Komlosh, P.J. Basser, Imaging local diffusive dynamics using diffusion exchange spectroscopy MRI, Phys. Rev. Lett. 118 (2017) 158003–6.

[36]    D. Benjamini, P.J. Basser, Use of marginal distributions constrained optimization (MADCO) for accelerated 2D MRI relaxometry and diffusometry, J. Magn. Reson. 271 (2016) 40–45.

[37]    L. Venkataramanan, Y.Q. Song, M.D. Hürlimann, Solving Fredholm integrals of the first kind with tensor product structure in 2 and 2.5 dimensions, IEEE Trans. Signal Process. 50 (2002) 1017–1026.

[38]    M.D. Hürlimann, L. Venkataramanan, Quantitative measurement of two-dimensional distribution functions of diffusion and relaxation in grossly inhomogeneous fields, J. Magn. Reson. 157 (2002) 31–42.

[39]    A.M. Olaru, J. Kowalski, V. Sethi, B. Blümich, Exchange relaxometry of flow at small Péclet numbers in a glass bead pack, J. Magn. Reson. 220 (2012) 32–44.

[40]    A. Papaioannou, R. Kausik, Methane storage in nanoporous media as observed via high-field NMR relaxometry, Phys. Rev. Appl. 4 (2015) 1–11.

[41]    K.-M. Song, J. Mitchell, H. Jaffel, L.F. Gladden, Monitoring water transport between pores and voids in aerated gypsum using two-dimensional nuclear magnetic resonance exchange measurements, J. Phys. D. Appl. Phys. 45 (2012) 105302–9.

[42]    J.D. Griffith, J. Mitchell, A.E. Bayly, M.L. Johns, Observing diffusive exchange between surfactant and aqueous domains in detergents, J. Phys. Chem. B. 113 (2009) 7156–7161.

[43]    K.E. Washburn, P.T. Callaghan, Tracking pore to pore exchange using relaxation exchange spectroscopy, Phys. Rev. Lett. 97 (2006) 25–28.

[44]    J.H. Lee, C. Labadie, C.S. Springer, G.S. Harbison, Two-dimensional inverse Laplace transform NMR: altered relaxation times allow detection of exchange correlation, J. Am. Chem. Soc. 115 (1993) 7761–7764.

[45]    R. Ernst, Richard, G. Bodenhausen, A. Wokaun, Principles of nuclear magnetic resonance in one and two dimensions Vol. 14, 1987.

[46]    H.M. McConnell, Reaction rates by nuclear magnetic resonance, J. Chem. Phys. 28 (1958) 430–431.

[47]    M.H. Levitt, Spin Dynamics: Basics of Nuclear Magnetic Resonance, John Wiley & Sons, West Sussex, UK, 2008.

[48]    M. Van Landeghem, A. Haber, J.-B. D'Espinose De Lacaillerie, B. Blumich, Analysis of multisite 2D relaxation exchange NMR, Concepts Magn. Reson. 88 (2010) 153–169.

[49]    R.D. Dortch, R.A. Horch, M.D. Does, Development, simulation, and validation of

NMR relaxation-based exchange measurements, J. Chem. Phys. 131 (2009) 164502–11.

[50] J. Kolz, Y. Yarovoy, J. Mitchell, M.L. Johns, L.F. Gladden, Interactions of binary liquid mixtures with polysaccharides studied using multi-dimensional NMR relaxation time measurements, Polymer (Guildf). 51 (2010) 4103–4109.

[51] R.P. Choudhury, M. Schönhoff, Pulsed field gradient NMR study of phenol binding and exchange in dispersions of hollow polyelectrolyte capsules, J. Chem. Phys. 127 (2007) 234702–9.

[52] L. Monteilhet, J.P. Korb, J. Mitchell, P.J. McDonald, Observation of exchange of micropore water in cement pastes by two-dimensional $T_2$-$T_2$ nuclear magnetic resonance relaxometry, Phys. Rev. E - Stat. Nonlinear, Soft Matter Phys. 74 (2006) 1–9.

[53] L.M. Burcaw, M.W. Hunter, P.T. Callaghan, Propagator-resolved 2D exchange in porous media in the inhomogeneous magnetic field, J. Magn. Reson. 205 (2010) 209–215.

[54] R. Bai, D. Benjamini, J. Cheng, P.J. Basser, Fast, accurate 2D-MR relaxation exchange spectroscopy (REXSY): beyond compressed sensing, J. Chem. Phys. 145 (2016) 154202–14.

[55] R. Bai, A. Cloninger, W. Czaja, P.J. Basser, Efficient 2D MRI relaxometry using compressed sensing, J. Magn. Reson. 255 (2015) 88–99.

[56] M.N. d'Eurydice, E.T. Montrazi, C.A. Fortulan, T.J. Bonagamba, $T_2$-filtered $T_2$-$T_2$ exchange NMR, J. Chem. Phys. 144 (2016) 204201–10.

[57] J.A. Aguilar, M. Nilsson, G. Bodenhausen, G.A. Morris, Spin echo NMR spectra without J modulation, Chem. Commun. 48 (2012) 811–813.

[58] G.H. Golub, M. Heath, G. Wahba, Generalized cross-validation as a method for choosing a good ridge parameter, Technometrics. 21 (1979) 215–223.

[59] M.D. Hürlimann, Effective gradients in porous media due to susceptibility differences, J. Magn. Reson. 131 (1998) 232–40.

# z-T$_2$-T$_2$ provides higher resolution of cross-peaks
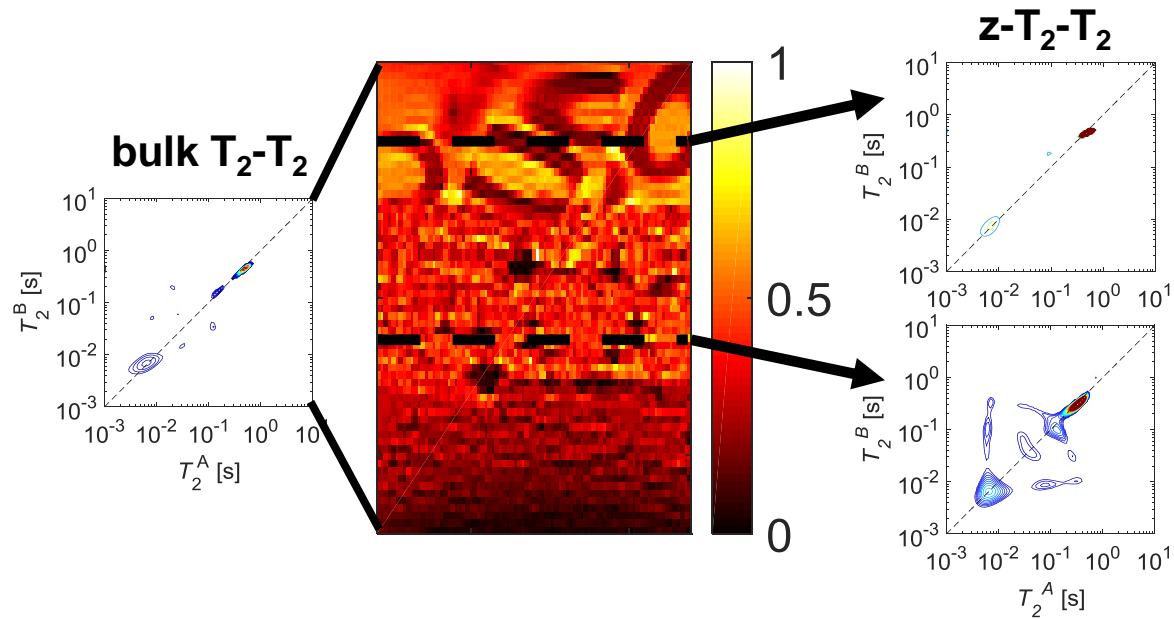


**bulk T$_2$-T$_2$**

**z-T$_2$-T$_2$**

**Highlights:**

- Spatially-resolved relaxation-exchange correlation technique $(z - T_2 - T_2)$ introduced.
- $z - T_2 - T_2$ method validated against bulk $T_2 - T_2$.
- Frequency-encoding MRI scheme enables same experimental duration as in $T_2 - T_2$.
- Local $z - T_2 - T_2$ spectra enable higher cross-peak resolution than $T_2 - T_2$ ones.
- $z - T_2 - T_2$ aids the study of local intra- and inter-particle mass transfer.